npj | clean water

Article

Published in partnership with King Fahd University of Petroleum & Minerals

https://doi.org/10.1038/s41545-024-00404-8

Turning mine-tailing streams into sources of water and mineral salts in a membrane-sustained circular scenario

Enrica Fontananova[1] ✉, Elvira Pantuso[1], Laura Donato[1], Elisa Esposito[1], Rosanna Rizzi[2], Rocco Caliandro[2] & Gianluca Di Profio[1] ✉

The discharge of wastewater from the mining industry has a critical ecological impact, potentially endangering both soil and marine ecosystems. Alternatively, recovering pure water and valuable materials from these hypersaline streams through a technologically efficient process, would help reduce the ecological impact of the waste, while providing a viable supply chain for raw materials such as magnesium, potassium and others, considered critical to the economy. In this context, this work aimed to simultaneously recover pure water and mineral salts from mine wastewater by membrane-assisted crystallization (MAC). A prior theoretical study based on thermodynamic parameters attempted to predict salts precipitation at different temperatures. MAC tests were then performed at specific thermal gradients and feed pretreatment conditions, achieving preferential precipitation of solids products of different composition containing large quantities of Ca or Mg/K minerals from the real mine tailing wastewater. The experiments also demonstrated the central impact of heterogeneous nucleation effects.

The growing global consumption of natural resources, under the pressure of continuous population growth and the expansion of emerging economies, has accentuated the impact of human activities on the environment[1]. As an ultimate consequence, many of the raw materials essential to the economy are limited[2] and natural resources necessary for human life, such as water[3], are stressed in ever larger areas of the world[4]. In this context, the paradigm shift from the current linear economy based on the extract—produce—use—dispose model, towards a closing loop circular economy scenario built on the concept of total recovery of raw materials, is seen as a viable solution for environmentally sustainable growth that combines economic development with social needs[5].

Today, most materials used in industry, technological development and energy generation are extracted through mining[6]. Mining has historically been a major source of wastes, most often in the form of wet slurries that are conventionally disposed of in tailings dams. It is estimated that there are approximately 18,000 metal and mineral extraction dams in the world, of which 3,500 are still active, (https://earthworks.org) that globally generate more than 14 billion tons per year of wastewater[7]. These highly salts concentrated effluents deliberately or accidentally contribute to significant pollution of river basins, resulting in serious risks to human health and long-term environmental implications[8] such as eutrophication[9], increased salinity or alkalinity of the soil and deterioration of the quality of soil where wastewater is used for irrigation[10].

However, in the context of natural resource recycling, mine-tailing wastewater can be considered as a potential source of water[11,12], minerals[13] and energy[14,15], if treated with efficient and sustainable technologies, while decreasing the environmental polluting potential of the mining activities[16]. Salts recovered from hypersaline streams can find application in several industrial fields such as metallurgical, fertilizer, ceramic, detergent or petrochemical[17,18]. For example, among many essential products widely used in industry, magnesium and potassium are considered critical raw materials for the European ecosystem, whose recovery from highly concentrated solutions represents a serious technological challenge[19–21].

On this basis, the main objective of this work was to demonstrate the possibility of valorizing wastewater deriving from mining activities through the recovery of pure water and mineral salts using membrane-assisted crystallization (MAC) technology[22]. MAC is an interesting separation technique that offers the possibility of obtaining a high recovery rate from hypersaline solutions whose salt concentration is well beyond the operating range of reverse osmosis (RO)[23–25], thus obtaining high-quality water[26] along with flexibility and suitability of integrated operations[27]. In one embodiment, it is based on the use of hydrophobic and porous membranes to contact the hot feed solution and the cold condensing fluid (normally water)

[1]Consiglio Nazionale delle Ricerche (CNR), Istituto per la Tecnologia delle Membrane (ITM), Via P. Bucci Cubo 17/C, 87036 Rende (CS), Italy. [2]Consiglio Nazionale delle Ricerche (CNR), Istituto di Cristallografia (IC), Via G. Amendola 122/O, 70126 Bari (BA), Italy. ✉e-mail: e.fontananova@itm.cnr.it; g.diprofio@itm.cnr.it

undergoing mass exchange in the vapor phase, driven by the vapor pressure difference generated by the thermal gradient between the two sides[22]. Specifically, because each pore on the membrane surface acts as a solvent removal point, supersaturation is generated uniformly across the entire membrane module. Therefore, compared to typical crystallization methods, MAC technology allows optimal control of the supersaturation level by acting on operating parameters such as temperature, flow rate and membrane module geometry, thus influencing crystal nucleation and growth rates, while it can be easily scaled-up thanks to the modularity of the membrane[16,28]. Although the application of MAC technology for the recovery of solid products from industrial waste effluents has been proposed in recent publications[29–31], these works are mainly linked to studies performed with synthetic model solutions and do not take into account the effect of multi-ionic composition and competitive precipitation kinetics from complex mixtures.

Here, we focused on real mine tailing wastewater extracted from the intersection point of the collector that picks up brines from different salt extraction industries in the region of Catalonia, which is located in Castellgalì (near Barcelona, Spain). In addition to being a stream of serious environmental impact that flows more than 162 km inland to the reception tank of the El Prat de Llobregat seawater reverse osmosis plant (SWRO), hypersaline waste is pumped 3 km offshore through a submarine outlet at the constant flow rate of 1800 m^3 per hour, with a potential impact also on the marine ecosystem. Given the complex nature of the stream, we first performed thermodynamic simulation work, aiming to predict the salts that can be recovered from the brine of known composition under different temperature conditions and at different solute concentration factors. Then, membrane-assisted crystallization experiments were first conducted using artificial hypersaline brine, to validate the predictive ability of the theoretical approach. Finally, real mine wastewater was tested as a feed with two different MAC configurations designed to study the effect of thermal gradients on the composition of the recovered crystalline salt product.

Results

Theoretical simulations and MAC tests with artificial brine

The first step of this study consisted of a theoretical simulation using PHREEQC software implementing the Pitzer model, with ionic compositions, density, and pH of the feed solutions reported in the Methods section as input parameters. The objective was to evaluate the predictive ability of the method based on a theoretical framework built on available thermodynamic data, to anticipate the species that can be recovered as a crystalline solid product from a multi-ionic solution such as mining wastewater. Once the saturation index (*SI*) at incremental concentration factors (*CF*) was calculated for all ionic combinations that could give rise to solid species at the specified temperature, membrane-assisted crystallization tests were performed with artificial feed solutions to compare theoretical and experimental results.

Figure 1A–C show the saturation profiles as a function of the concentration of the solution (up to *CF* 1.75) for the different species, while Table 1 reports the *SI* values at the final concentrations reached in the crystallization tests. At 31 °C (Fig. 1A), positive *SI* curves for six phases are shown over the entire range of solution concentrations, with the Ca/Mg-carbonates *huntite* and *dolomite* and the Ca/K-sulphate *gorgeyite* showing the highest saturation indices for *CF* > 1.4. The saturation curves for *magnesite*, *aragonite* and *calcite* always extend into the positive region of the graph, in the SI range of 1 to 2. Of note, the saturation curve for sodium chloride (*halite*) is negative for low concentrations, with a positive slope that brings the curve into the positive range for *CF* > 1.35; a similar behaviour is observed for calcium sulphates *anhydrite* and *gypsum*. Other mixed sulphates *glauberite* and *polyhalite* show positive *SI* values only for concentration factors higher than those obtained experimentally at the end of our tests.

Moving to 44 °C and 49 °C (Fig. 1B, C, respectively), a shift towards progressively higher *SI* values is observed for all species, with the exception of *gorgeyite*, which shows a decreasing solubility trend, *magnesite* and *halite*, which have both solubility curves that are less temperature dependent. Therefore, based on the simulations, at all temperatures a similar scenario is observed, where preferential precipitation of Ca, Mg or combined Ca/Mg carbonates and minor contribution of the Ca/K sulphates *gypsum* and *halite* is expected.

Membrane-assisted crystallization tests were performed with synthetic feed solutions of the composition shown in Table 5, up to the concentration factor displayed in Fig. 1 at different operating temperatures. The two configurations shown in Fig. 9 were used: the crystallization with the feed solution circulated at a fixed temperature of 49 °C (Fig. 9A), and the configuration with the feed circuit divided into two crystallization vessels held at 44 °C and 31 °C, respectively (Fig. 9B).

Microscopy analysis of the recovered solid samples indicates that the size and shape of the crystals are highly dependent on the operating temperature (Fig. 2A–F). At 31 and 44 °C, the crystal size distributions (*CSD*) show a bimodal profile (Figs. 2D, E), with the two most frequent crystal sizes at 9–11 and 17–19 μm, and the variation coefficient (*CV*) of 40.1% and 65.5%, respectively.

By increasing the crystallization temperature to 49 °C, the shape changes from the predominantly irregular habit (Fig. 2A) seen at lower temperature, to small cubes/square-based prisms (Fig. 2C) with monodisperse size distribution centered around 9 μm (Fig. 2F) and the *CV* of 44.2%.

The increase in *CV* for crystals obtained at 44 °C is explained by the increase in the inhomogeneity of the product, being composed of a mixture of multiple crystal species with different habits and aggregation, compared to experiments conducted at 31 °C and 49 °C, where the prevalence of a specific crystalline phase was obtained. EDX analyses suggest that the irregular crystals were composed mainly of $CaCO_3$ while the cubes/prisms were essentially NaCl.

Quantitative PXRD analysis of solid precipitates (Fig. 3A) obtained at the lowest temperature (31 °C) shows a mixture with *aragonite* as the main component (66.2%), a relatively low amount of *halite* (14.1%) and Mg-sulphates *pentahydrite* (6.5%), *kainite* (3.1%), *bloedite* (2.9%) and *kieserite* (1.8%) as minor components, with a small portion of *polyhalite* (3.1%) and *sylvite* (2.3%). As a result, the weight content of calcium in the recovered product exceeds 54% of all elements (Fig. 3B), being almost completely (~99%) included in the *aragonite* phase.

The precipitate recovered at 44 °C was a mixture composed mainly of *halite* (36.7%), with Ca-sulphate *glauberite* (23.5%), Ca/Mg sulphate *polyhalite* (9.5%) and Mg-sulphate *bloedite* (1.2%), and the carbonates *aragonite* (15%) and *huntite* (3.5%) along with a moderate amount of the K-salts *sylvite* (8.9%) and *arcanite* (1.7%). At 49 °C, a different composition of the precipitate was obtained, with 76.4% *halite*, some amounts of Mg-sulphates *kainite* (17.8%), *bloedite* (1.3%) and *kieserite* (1%) co-precipitated as secondary components with only a small amount of *aragonite* (3.5%).

The results indicated that within the relatively narrow range of temperatures explored in this work, a precipitate with a very different composition was recovered from the artificial feed, going from the prevalence of $CaCO_3$ at the lowest temperature, to the preferential precipitation of NaCl at the highest temperature. While the simulations were not effective in predicting the detailed composition of the solid precipitate, the theoretical work predicted the crystallization of sparingly soluble Ca phases, particularly at lower temperatures, despite the Ca^{2+} concentration in the starting solution was 6 times lower than that of Mg^{2+} ions. Therefore, with the aim of reducing the amount of Ca^{2+} ions, while minimizing the loss of Mg^{2+}, a basic feed treatment was performed by adding $NaHCO_3$ to precipitate calcium as $CaCO_3$ according to the following equilibria:

$$HCO_3^- \leftrightarrows CO_3^{2-} + H^+ \log K_{a1} = -10.33$$

$$Ca^{2+} + CO_3^{2-} \leftrightarrows CaCO_3 \log K_{a2} = -7.1$$

Based on the initial Ca^{2+} concentration, the $NaHCO_3$ solution was dosed at 70 °C under continuous stirring to obtain a molar ratio $[CO_3^{2-}]$/

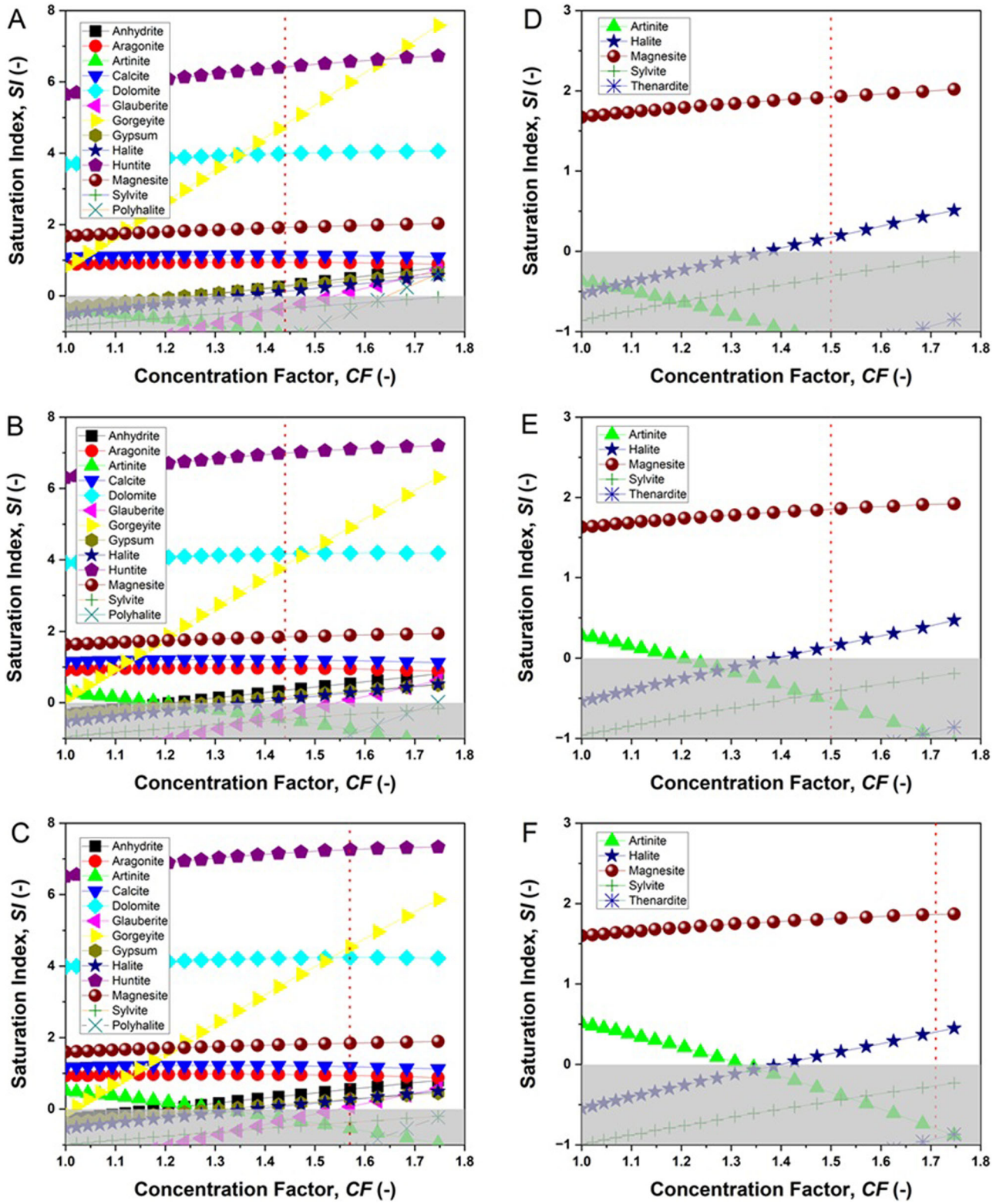

Fig. 1 | Simulations performed by PHQREEC software for synthetic solution. Simulated saturation index (SI) versus concentration factor (CF) for the synthetic hypersaline solution at 31 °C (**A**, **D**), 44 °C (**B**, **E**) and 49 °C (**C**, **F**), before (**A**–**C**) and after (**D**–**F**) basic treatment of the feed solution. The vertical lines show the concentration factor at the endpoint of the MAC tests. The shaded areas highlight the negative SI region. For simplicity, curves for SI < −1 are not shown.

$[Ca^{2+}] > 3$, adjusting the pH below 9 (with 1 M NaOH) to avoid the precipitation of $Mg(OH)_2$ (*brucite*), which occurs at pH>9.3[32]. As assessed by IC analysis, the basic treatment allowed the quantitative removal of Ca^{2+} with the loss of Mg^{2+} around 5% wt. With the new composition of the solution obtained after the basic treatment (shown in Table 5), the saturation curves for the three operating temperatures of interest were simulated again (Fig. 1D–F). The corresponding *SI* values at the concentration factors achieved at the end of the MAC tests are shown in Table 1. Under these conditions, *magnesite* and *halite* were the only phases showing positive saturation values for $CF > 1.4$. Also in this case, the

Table 1 | Saturation index (*SI*) values simulated at the final concentration factor (*CF*) obtained in MAC tests performed at different temperatures for the synthetic hypersaline solution before (Syn) and after (BT) the basic treatment (numbers in bold are referred to the species that were actually detected in the solid precipitate by PXRD analysis)

Phase	Formula	Saturation Index					
		31 °C		44 °C		49 °C	
		Syn.[(a)]	BT[(b)]	Syn.[(a)]	BT[(b)]	Syn.[(c)]	BT[(d)]
Huntite	$CaMg_3(CO_3)_4$	6.40	–	**6.98**	–	7.26	–
Gorgeyite	$K_2Ca_5(SO_4)_6{\cdot}H_2O$	4.69	–	3.74	–	4.54	–
Dolomite	$CaMg(CO_3)_2$	3.98	–	4.17	–	4.24	–
Magnesite	$MgCO_3$	1.91	1.93	1.84	**1.86**	1.84	1.86
Calcite	$CaCO_3$	1.15	–	1.20	–	1.19	–
Aragonite	$CaCO_3$	**0.95**	–	**0.97**	–	**0.94**	–
Anhydrite	$CaSO_4$	0.26	–	0.33	–	0.56	–
Gypsum	$CaSO_4{\cdot}2H_2O$	0.23	–	0.15	–	0.28	–
Halite	NaCl	**0.11**	**0.20**	**0.08**	**0.17**	**0.26**	**0.37**
Sylvite	KCl	**−0.37**	**−0.29**	**−0.48**	**−0.40**	−0.37	**−0.29**
Glauberite	$Na_2Ca(SO_4)_2$	−0.37	–	**−0.35**	–	0.07	–
Artinite	$Mg_2CO_3(OH)_2{\cdot}3H_2O$	−1.04	**−1.18**	−0.44	−0.59	−0.55	**−0.74**
Thenardite	Na_2SO_4	–	−1.23	--	−1.20	–	−0.96
Polyhalite	$K_2MgCa_2(SO_4)_4{\cdot}2H_2O$	**−1.31**	–	**−1.70**	–	−1.12	–
Epsomite	$MgSO_4{\cdot}7H_2O$	–	−1.86	–	**−2.07**	–	−2.05
Hexahydrite	$MgSO_4{\cdot}6H_2O$	–	**−1.91**	–	−2.02	–	−1.93
Arcanite	K_2SO_4	−2.11	**−2.00**	**−2.25**	−2.14	−2.19	−2.07
Pentahydrite	$MgSO_4{\cdot}5H_2O$	**−2.18**	**−2.05**	−2.32	**−2.19**	−2.23	−2.08
Kainite	$KMgClSO_4{\cdot}3H_2O$	**−2.37**	−2.14	−2.51	**−2.28**	**−2.23**	**−1.97**
Kieserite	$MgSO_4{\cdot}H_2O$	**−2.48**	−2.29	−2.36	−2.18	**−2.06**	**−1.85**
Bloedite	$Na_2Mg(SO_4)_2{\cdot}4H_2O$	**−2.68**	−2.37	**−2.85**	**−2.56**	**−2.54**	**−2.21**

CF: (a) 1.44, (b) 1.50, (c) 1.57, (d) 1.71

simulations did not predict substantial differences at the three different temperatures.

Morphological analyses of the precipitates showed that bounded needle-like crystals were the most frequently observed shape at the lowest temperature, the composition of which contains relatively high amounts of magnesium (Fig. 2G). By increasing the crystallization temperature, the size of the crystals does not change significantly, remaining around 14 μm as the most frequent value (Fig. 2J–L), while the *CSD* is rather large, with *CV* of 75.4%, 80.1% and 46.4% at 31 °C, 44 °C, and 49 °C, respectively.

PXRD analysis of the solid precipitates (Fig. 3C) revealed that at 31 °C the most abundant component was *arcanite* (38.1%), with the Mg sulfates *pentahydrite* (25.2%) and *hexahydrite* (17.4%) and Mg carbonate *artinite* (9.1%) (tiny needle-like crystals shown in Fig. 2G) as the main magnesium-containing phases, while *halite* (8.2%) and *sylvite* (2%) were obtained as additional components. In these conditions the solid product mainly contains magnesium (14.7%), potassium (38.1%) and sulfur (27.9%), together with smaller quantities of chlorine (12.4%) and sodium (6.8%) (Fig. 3D).

The precipitates obtained at 44 °C and 49 °C were mainly composed of NaCl, with components containing Mg (mainly sulfates) decreasing their contribution with increasing temperature. At 49 °C, the amount of *halite* (Fig. 2I) reached approximately 91% with only minor amounts of Mg sulfates (~7%) and carbonates (~2%). In particular, while at the highest temperatures the basic pretreatment did not substantially influence the composition of the precipitate compared to the untreated feed, the crystalline product obtained at the lowest temperature turned from a solid containing predominantly calcium into a product composed of an excess of magnesium and potassium.

Experiments with real mine-tailing wastewater

The mining wastewater extracted from the collector in the district of Castelgalì (Spain), was fed to the MAC equipment of Fig. 9. The preventive evaluation of the actual composition of the feed by ion chromatography (Table 5) was necessary to simulate the *SI* vs. *CF* curves at the crystallization temperatures of interest for this work (Fig. 4A–C) from PHREEQC software. The values of *SI* at the final solution concentration obtained in crystallization tests are given in Table 2. The simulations described a similar situation for the real feed compared to the artificial solution (Fig. 1A–C) before the basic treatment, with the slight downward translation for all curves, due to the lower magnesium content. Given the similarity in ionic composition and saturation curves, the crystallization result was also expected to be comparable at all temperatures. Therefore, Ca/Mg carbonates *huntite*, *dolomite*, *magnesite*, *calcite*, *aragonite*, and K/Ca-sulphate *gorgeyite* are expected to precipitate from real solutions, with the appearance of sulphates *anhydrite*, *gypsum*, *glauberite*, and *halite* showing a reduced thermodynamic tendency to appear.

Similar to what was observed with artificial solutions, crystallization from real wastewater produced at 31 °C mainly aggregated and irregularly shaped particles with bimodal size distribution (Figs. 5A, D) and a coefficient of variation of 54.3%. At 44 °C, the number of irregular crystals decreased while small cubes appeared with the crystal size decreasing to ~10 μm and *CV* of 39.5% (Fig. 5B, E). The precipitates obtained at 49 °C were mainly composed of NaCl cubes less than 10 μm in size (Fig. 5F), with some aggregated prismatic crystals of high aspect ratio and containing calcium and sulfur (Fig. 5C).

Based on PXRD analyses, crystals precipitated from the real feed at the lowest temperature (31 °C) contain >87% *aragonite* (Fig. 6A) and

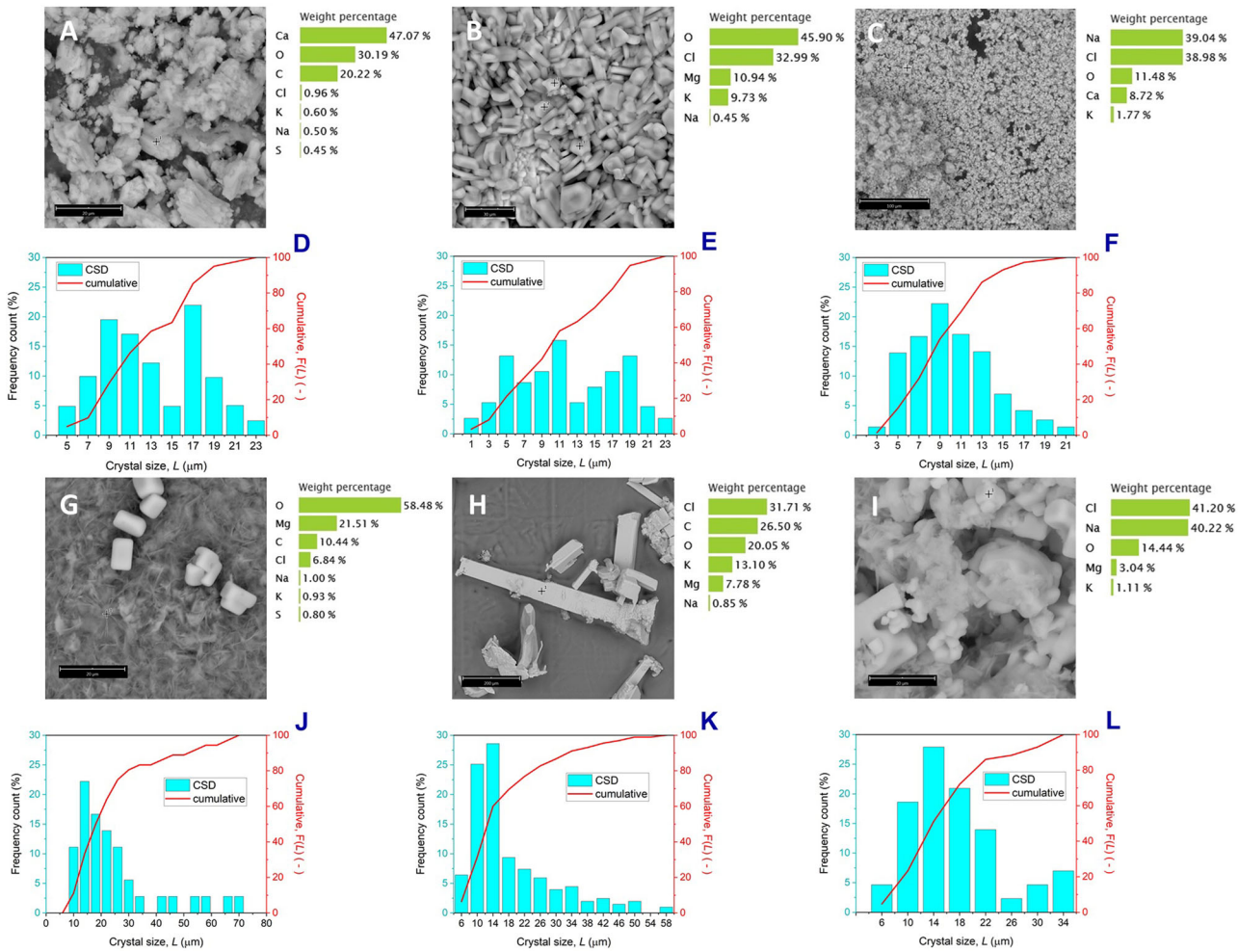

Fig. 2 | Morphology characterization of crystalline solids from synthetic solution. Crystals recovered at the end of MAC tests (28 h) from synthetic hypersaline feed at 31 °C (**A**, **D**), 44 °C (**B**, **E**) and 49 °C (**C**, **F**): scanning electron micrographs with element composition determined by EDX (**A**–**C**) and crystal size distribution calculated by elaborating the optical microscopy images (**D**–**F**). Crystals recovered from synthetic feed after basic treatment at 31 °C (**G**, **J**), 44 °C (**H**, **K**) and 49 °C (**I**, **L**): scanning electron micrographs with element composition determined by EDX (**G**–**I**) and crystal size distribution calculated using optical microscope images (**J**–**L**). The SEM images were taken randomly at various points of the samples and do not necessarily represent the most frequent morphology of the crystals that make up the precipitates.

approximately 10% *gypsum*, with *kieserite* (1.8%) and *halite* (1%) as minor components. This allows recovery of a solid product containing >91 wt.% calcium (Fig. 6B). By increasing the crystallization temperature, the amount of *aragonite* progressively decreases (45.5% at 44 °C and 8% at 49 °C), while the NaCl content increases correspondingly to 39.5% and 69.8%, respectively, with a certain amount of *gypsum* found at the highest temperature (Fig. 5C).

The basic treatment of the real feed proved to be less effective in removing calcium compared to the synthetic case, allowing the Ca^{2+} content to be reduced by >80% wt., with a loss of Mg^{2+} quantifiable as ~30% wt. The new solution composition reported in Table 5 was used as input to simulate the saturation curves of Fig. 4D–F. Due to incomplete Ca^{2+} removal, the simulations for treated and untreated wastewater appear very similar, with the notable shift towards higher *SI* values for all Ca/Mg carbonates *artinite*, *calcite*, *aragonite*, *magnesite*, *dolomite* and *huntite*, and downward migration to lower *SI* for the curves of sulfates *goergeyite*, *anhydrite*, *gypsum*, *glauberite* and for *halite*.

The crystals obtained at 31 °C were heterogeneous in shape, with a typical size distribution centered around 26 μm (Fig. 5J), probably due to some aggregation, and *CV* of 30.2%. At 44 °C the particle size distribution of the crystals worsens (Fig. 5K), reaching a *CV* of 72.8% with a heterogeneous composition of different particle shapes and sizes. For a crystallization temperature of 49 °C, the precipitate was consistent with an increased amount of NaCl cubes, embedded to some extent within bounces of Mg-rich needles (Fig. 5I), and a *CSD* with a *CV* of 53.6%, centered around 14 μm (Fig. 5L).

Based on PXRD analysis, it was shown that calcium-containing phases were still obtained (Fig. 6C), despite the treatment step, due to incomplete removal of Ca^{2+}. At the lowest temperature, the product was composed of a mixture of many salts including Ca/Mg sulfates *pentahydrite* (18.6%), *bloedite* (14.6%), *polyhalite* (12.1%), *kainite* (7 .6%) and *kieserite* (1.6%) and K phases *arcanite* (11.3%) and *sylvite* (2.8%), with *halite* (12.2%) and *aragonite* (19.2%), so that similar amounts of calcium (18%), potassium (18%), chlorine (19%) and sulfur (22.6%) were obtained, with a magnesium content of 9.2% (Fig. 6D).

By increasing the temperature to 44 °C, Ca/Mg sulfates were still the dominant species with *glauberite* (30.8%), Mg and Mg/Ca sulfates *kieserite* (8.4%), *bloedite* (7%), *pentahydrite* (6%), *polyhalite* (6.1%) and Ca and Mg carbonates *huntite* (5.6%), *dolomite* (5%) and *aragonite* (4.5%), with *halite* (22.3%) and *sylvite* (4.3%). This allowed us to recover a solid product containing 14.7% calcium (about 84% less than real untreated feed) and 8% magnesium. At the highest temperature, excessive *halite* precipitation (~ 67%) provided a solid product containing mainly sodium and chlorine and a small amount of magnesium (6.9%), included mainly in *artinite* crystals (Fig. 5I).

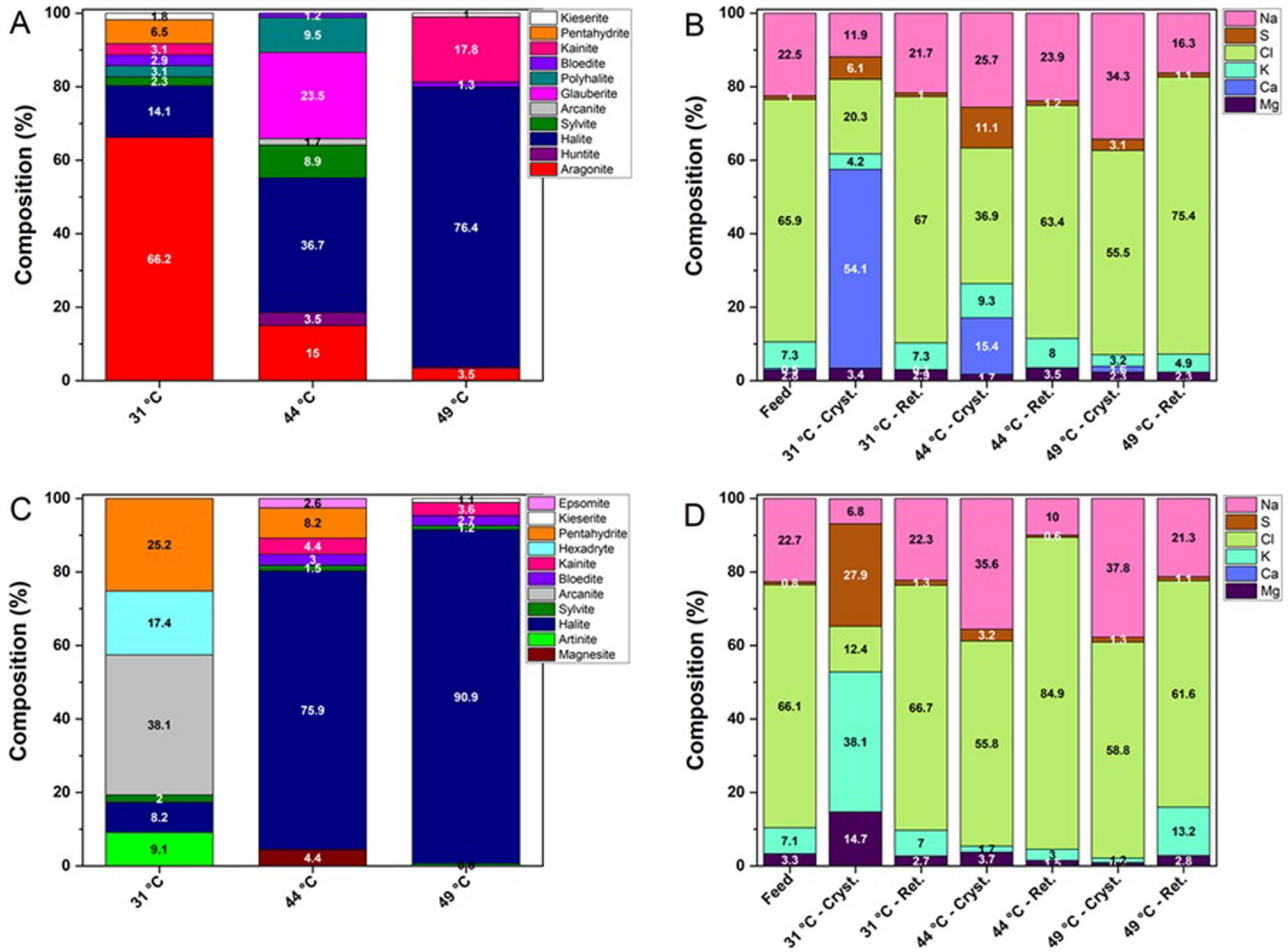

Fig. 3 | Quantitative composition of the solid precipitates for synthetic solution. Compositions obtained before (**A**, **B**) and after (**C**, **D**) the basic treatment of synthetic hypersaline solution at different temperatures, in terms of crystalline phases detected by PXRD (**A**, **C**) and corresponding relative elemental composition (excluding C, O and H atoms) (**B**, **D**) in the starting solution (Feed), recovered crystals (Cryst.) and mother solution after removal of crystals by filtration (Ret.).

Discussion

Quantitative and qualitative analysis of the solid precipitates recovered after the MAC experiments revealed that for both synthetic and real untreated solutions, $CaCO_3$ was the most abundant phase at the lowest temperature (31 °C), while the prevalence of NaCl was observed at 49 °C. This result is inconsistent with the simulations that generated the highest saturation curves reported in Fig. 1A–C and Fig. 4A–C for *huntite*, *dolomite*, *goergeyite* and *magnesite*, without substantial variations across the temperature range investigated, while these species were hardly obtained in crystallization tests. Furthermore, the saturation curves of *halite* always lie below those of the $CaCO_3$ polymorphs *calcite* and *aragonite*, with the solubility of NaCl slightly increasing with temperature and that of $CaCO_3$ decreasing to some extent. In particular, among the anhydrous polymorphs of $CaCO_3$, the metastable *aragonite* phase was obtained selectively for all conditions, although *calcite* is the most stable form at the temperatures considered[33].

The exclusive formation of *aragonite* can be explained by the contribution of surface energy to the Gibbs free energy barrier for nucleation in the presence of relatively high concentrations of Mg^{2+} ions in solution[34–36]. It is known that for the concentration ratios $[Mg^{2+}]/[Ca^{2+}] > 2$, the increase in surface energy due to the adsorption of Mg^{2+} onto *calcite* increases the nucleation energy barrier, thus drastically inhibiting *calcite* formation[37,38]. In our study, the ratio $[Mg^{2+}]/[Ca^{2+}]$ was ~6 in synthetic feed and ~5 in real wastewater, thus influencing polymorphic selection towards the formation of the metastable *aragonite* phase. The higher recovery of $CaCO_3$ for the real feed compared to the synthetic solution is due to the higher initial Ca^{2+} concentration (~ 10%) and the larger concentration factor achieved at the end of the crystallization tests with real wastewater.

Similar to untreated feed solutions, MAC experiments with basic-treated hypersaline solutions provided a progressively increasing amount of *halite* as temperature increased, although the saturation curves of Fig. 1D–F and Fig. 4D–F suggested the crystallization of *magnesite* as the main magnesium-containing solid component. Furthermore, Mg-containing hydrated phases *pentahydrite*, *hexahydrite*, *bloedite*, *polyhalite*, *kainite* and *artinite* were obtained despite their low saturation curves. In this case, quantitative calcium removal was crucial to increase the amount of magnesium recovered from crystallization processes, as demonstrated by the precipitation of significant amounts of calcium sulphates from real wastewater, due to incomplete removal of Ca^{2+} ions.

In the case of synthetic feed, the complete removal of Ca^{2+} allowed the recovery at the lowest temperature of a solid product enriched in Mg (14.7%) and K (38.1%), which precipitated mostly as sulphates, while at 49 °C the preferential precipitation of NaCl with a purity greater than 91% by weight was obtained. In addition to the possible intrinsic limitations of the theoretical model implemented for such complex multi-ionic solutions, the substantial inconsistency between the simulated saturation curves and the actual composition of the precipitates cannot be explained on a purely thermodynamic ground, suggesting that crystallization in MAC experiments is controlled by kinetics rather than thermodynamics, where temperature plays an important role to achieve effective results.

According to the classical nucleation theory (CNT)[39], the formation of a new thermodynamic solid phase from a solution (homogeneous) is an

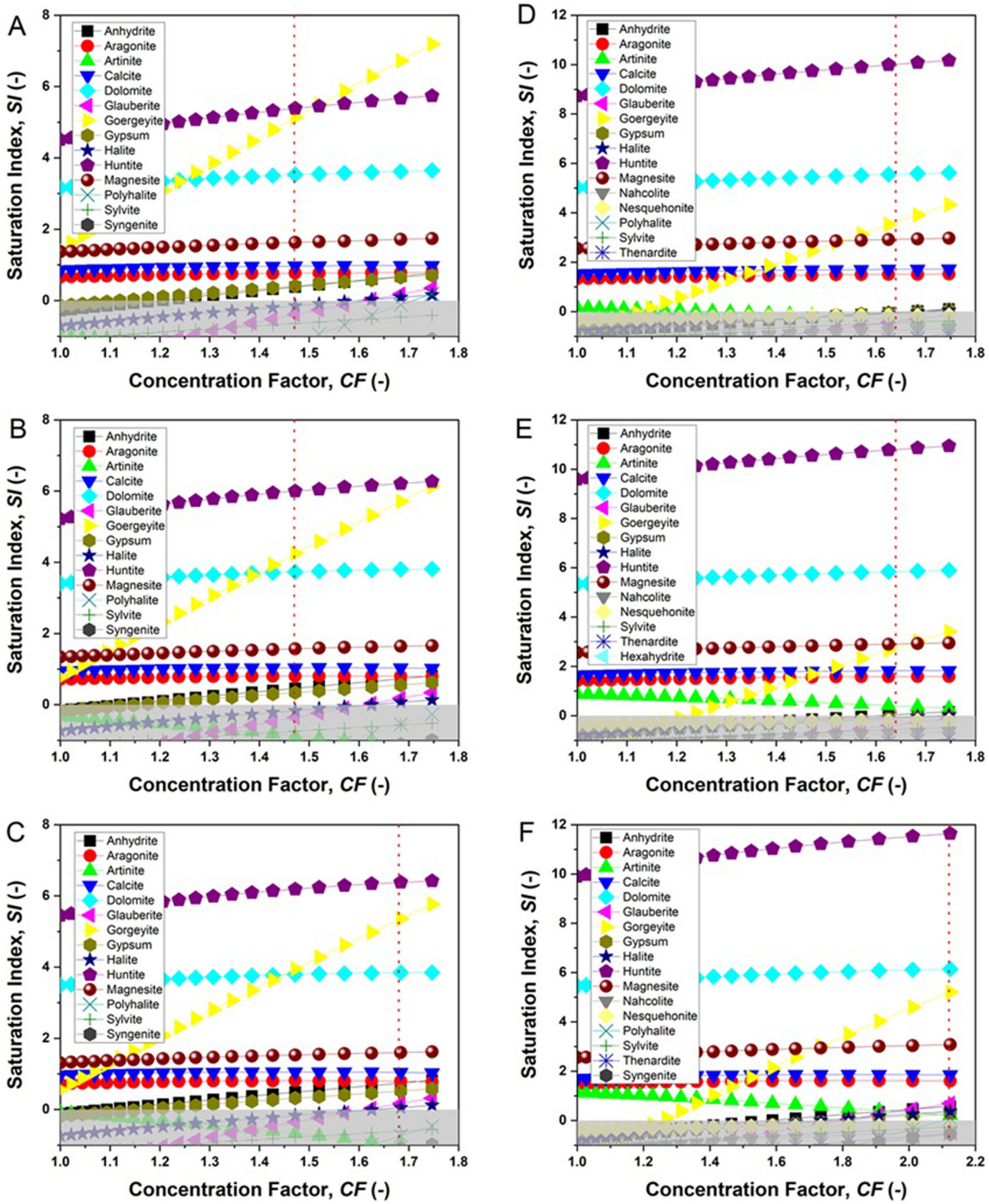

Fig. 4 | Simulations performed by PHQREEC software for real solution. Simulated saturation index (SI) versus concentration factor (CF) for real wastewater at 31 °C (**A**, **D**), 44 °C (**B**, **E**) and 49 °C (**C**, **F**), before (**A**–**C**) and after (**D**–**F**) the basic treatment of the feed solution. The vertical lines show the concentration factor at the endpoint of the MAC tests. The shaded areas highlight the negative SI region. For simplicity, curves with SI < −1 are not shown.

activated process whose energy barrier (ΔG^*_{HON}) is given by:

$$\Delta G^*_{HON} = \frac{16\pi\gamma^3_{ln}\Omega^2}{3(k_B T\sigma)^2} \quad (1)$$

where γ_{ln} [J/m^2] is the interfacial energy between the liquid and the nucleus, k_B is the Boltzmann constant (1.38×10^{-23} J K^{-1}), T [K] is the absolute temperature, Ω [m^3] is the volume of a crystal unit (i.e., the molar volume divided by the Avogadro's number), and σ is the

Table 2 | Saturation index (*SI*) values simulated at the final concentration factor (*CF*) obtained in MAC tests performed at different temperatures for real mine tailings wastewater before (Real) and after (BT) basic treatment (numbers in bold refer to the species that were actually detected in the solid precipitate by PXRD analysis)

Phase	Formula	Saturation Index					
		31 °C		44 °C		49 °C	
		Real[(a)]	BT[(b)]	Real[(a)]	BT[(b)]	Real[(c)]	BT[(d)]
Huntite	$CaMg_3(CO_3)_4$	5.39	**9.99**	**6.00**	**10.78**	**6.38**	**11.64**
Gorgeyite	$K_2Ca_5(SO_4)_6{\cdot}H_2O$	5.13	3.52	4.25	2.66	5.36	5.21
Dolomite	$CaMg(CO_3)_2$	3.53	5.55	3.73	**5.84**	3.85	6.14
Magnesite	$MgCO_3$	1.63	2.92	1.57	2.90	1.60	3.08
Calcite	$CaCO_3$	0.97	1.71	1.03	1.82	1.04	1.85
Aragonite	$CaCO_3$	**0.77**	**1.51**	**0.80**	**1.58**	**0.79**	1.60
Gypsum	$CaSO_4{\cdot}2H_2O$	**0.41**	−0.04	0.34	−0.10	**0.52**	0.26
Anhydrite	$CaSO_4$	0.38	−0.05	0.46	0.03	0.74	0.57
Halite	NaCl	**−0.15**	**−0.08**	**−0.17**	**−0.10**	**0.05**	**0.37**
Nesquehonite	$MgCO_3{\cdot}3H_2O$	–	−0.16	–	−0.22	–	−0.24
Glauberite	$Na_2Ca(SO_4)_2$	−0.39	−0.45	−0.36	**−0.40**	0.17	0.69
Sylvite	KCl	−0.64	−0.47	**−0.74**	**−0.58**	**−0.61**	**−0.26**
Nahcolite	$NaHCO_3$	–	−0.76	–	−0.72	–	−0.43
Thenardite	Na_2SO_4	–	−1.14	–	−1.09	–	−0.53
Polyhalite	$K_2MgCa_2(SO_4)_4{\cdot}2H_2O$	−1.18	**−1.38**	**−1.53**	**−1.70**	**−0.74**	0.09
Artinite	$Mg_2CO_3(OH)_2{\cdot}3H_2O$	−1.49	**−0.29**	−0.88	0.41	−0.98	**0.21**
Arcanite	K_2SO_4	–	**−1.72**	–	−1.84	–	−1.58
Hexadryte	$MgSO_4{\cdot}6H_2O$	–	−1.77	–	−1.85	–	**−1.55**
Pentahydrite	$MgSO_4{\cdot}5H_2O$	−2.02	**−1.94**	**−2.15**	**−2.06**	−2.00	**−1.71**
Kieserite	$MgSO_4{\cdot}H_2O$	**−2.43**	**−2.33**	−2.31	**−2.19**	−1.94	**−1.48**
Kainite	$KMgClSO_4{\cdot}3H_2O$	−2.54	**−2.28**	**−2.66**	−2.40	**−2.29**	**−1.57**
Bloedite	$Na_2Mg(SO_4)_2{\cdot}4H_2O$	−2.69	**−2.08**	**−2.84**	**−2.36**	**−2.42**	**−1.40**

CF: (a) 1.47, (b) 1.64, (c) 1.68, (d) 2.12

chemical potential difference, that is defined as:

$$\sigma = \ln\left(\frac{\mathrm{IAP}}{\mathrm{K_{sp}}}\right) \tag{2}$$

The nucleation rate N (number of nuclei per unit volume per unit time), can be expressed by:

$$N = A \cdot \exp\left(-\frac{\Delta G^*}{k_B T}\right) \tag{3}$$

where A [m^{-3} s^{-1}] is a kinetics factor[40].

Possible kinetics contributions can be exemplified by estimating the Gibbs free energy barrier for nucleation (ΔG^*) and comparing it to the k_BT term, since the magnitude of the energy barrier with respect to this thermal energy is a crucial factor in determining the number and nature of particles produced[41]. Based on Eq. 1 & 2, for a constant ion activity product, temperature influences the nucleation energy via inverse quadratic proportionality with the k_BT term and via the temperature dependence of K_{sp}. However, in the temperature range considered in this study, the slopes of the solubility curves for both $CaCO_3$ and NaCl are rather flat, while the increase in thermal energy is only 6% going from 31 °C to 49 °C.

Therefore, using literature data for γ_{ln} and Ω[38,42], we calculated the homogeneous nucleation (HON) energy barrier for *aragonite* and *halite* at different temperatures. The data are reported in Table 3 and show that at 31 °C, ΔG^*_{HON} of *aragonite* and *halite* is of the same order of magnitude for the untreated synthetic solutions, while NaCl is unsaturated for the real feed. Moving to 49 °C, the energy barrier of *aragonite* decreases by 14% and 20% for synthetic and real solutions respectively, while that of *halite* decreases by approximately 85% for synthetic solutions while in real wastewater the *halite* becomes saturated. Therefore, at such temperature, the nucleation barrier of *aragonite* becomes 25 and 1.5 times larger than that of *halite* for synthetic and real feeds, respectively, thus justifying the preferential precipitation of NaCl at the higher temperature.

For basic-treated synthetic solutions, complete removal of Ca^{2+} ions by precipitation as $CaCO_3$, allowed crystallization at the lower temperature of hydrated Mg sulphates. By moving to 49 °C, the energy barrier of *halite* decreased by 75%. For real solutions, the precipitation of *aragonite* at 31 °C was due to incomplete removal of Ca^{2+}, while *halite* was unsaturated. At 49 °C, although the energy barrier of *aragonite* is decreased by ~25%, *halite* becomes saturated with the ratio $\Delta G^*_{HON,aragonite}/\Delta G^*_{HON,halite} \sim 18$. Based on these calculations, the different precipitation trends of $CaCO_3$ and NaCl within the investigated temperature range could be explained by the undersaturation of NaCl at the lower temperature and by the lower nucleation energy barrier for *halite* at 49 °C.

Inspection of the membrane at the end of the MAC tests revealed that the surface was covered with a thin layer of loosely attached crystals. This crystalline product was completely recovered by rinsing the membrane with the retentate, leaving the surface clean, as shown by SEM analysis (Fig. 7). This observation supports the hypothesis that the crystals did not nucleate heterogeneously on the membrane but were eventually formed in the bulk solution and then deposited on the membrane surface, transported by the flowing liquid. However, the data in Table 3 indicate that for all conditions,

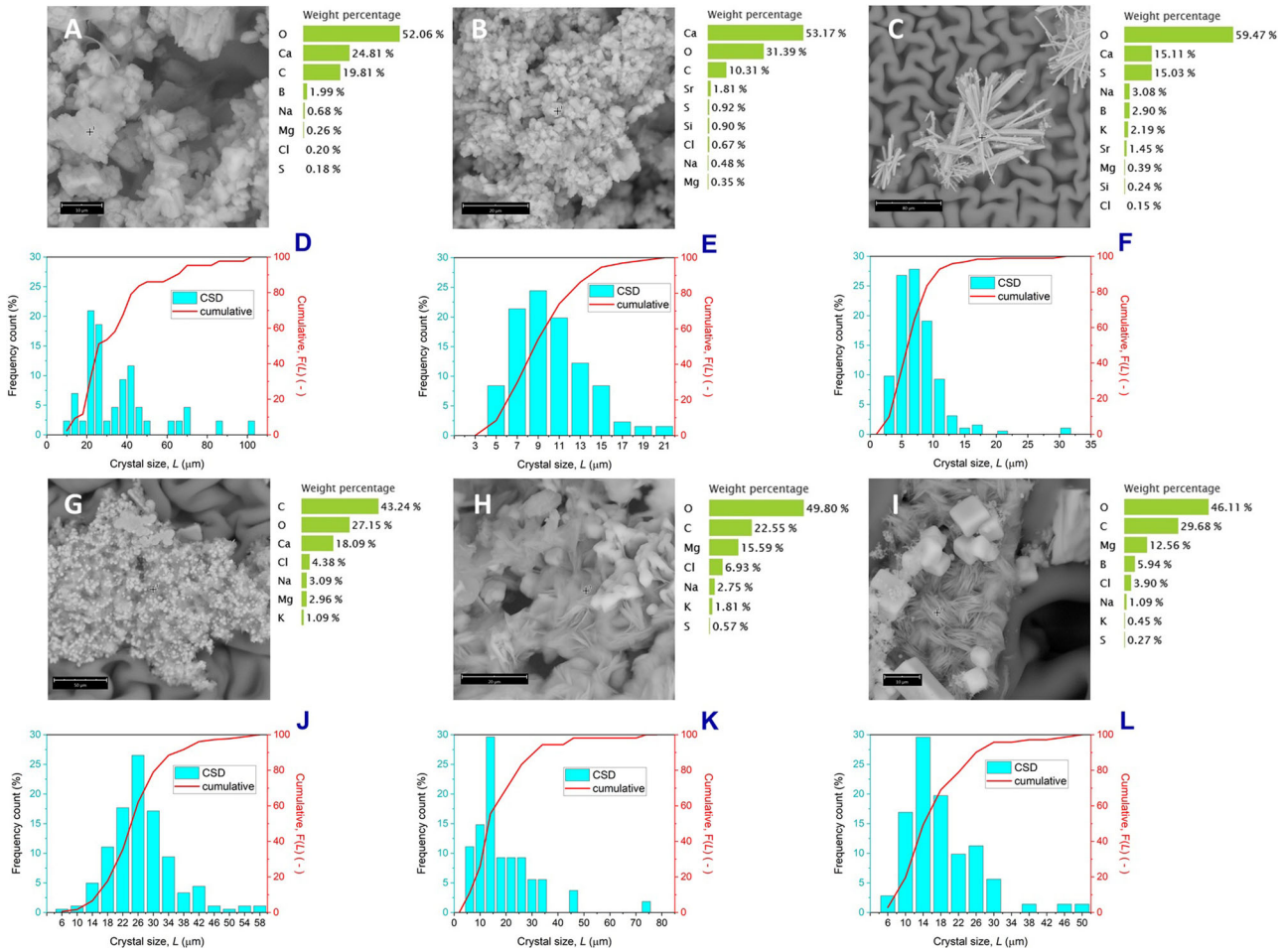

Fig. 5 | Morphology characterization of crystalline solids from real solution. Crystals recovered at the end of MAC tests (28 h) from real mine wastewater at 31 °C (**A**, **D**), 44 °C (**B**, **E**) and 49 °C (**C**, **F**): scanning electron micrographs with element composition determined by EDX (**A**–**C**) and crystal size distribution calculated by optical microscopy images (**D**–**F**). Crystals recovered from synthetic feed after basic treatment at 31 °C (**G**, **J**), 44 °C (**H**, **K**) and 49 °C (**I**, **L**): scanning electron micrographs with element composition determined by EDX (**G**–**I**) and crystal size distribution calculated using optical microscope images (**J**–**L**). The SEM images are taken randomly at various points of the samples and do not necessarily represent the most frequent morphology of the crystals that make up the precipitates.

ΔG^*_{HON} is from 3 to 4 orders of magnitude larger than k_BT, suggesting that the hypothesis that nuclei have enough thermal energy to grow beyond the critical size, thus exceeding the energy barrier for homogeneous nucleation, is rather questionable[43].

Furthermore, heterogeneous nucleation on the membrane surface and/or on other exogenous surfaces present in the bulk solution (such as impurities or colloidal particles), is much more common than homogeneous one[44] and could substantially contribute to reducing the energy barrier and its temperature dependence. The free energy barrier for heterogeneous nucleation (ΔG^*_{HEN}) is related to the homogeneous term by the following relation, valid for porous surfaces[45]:

$$\Delta G^*_{HEN} = \Delta G^*_{HON}\left[\frac{1}{4}(1-\cos\theta)^2(2+\cos\theta)\right]\left[1-\varepsilon\frac{(1+\cos\theta)^2}{(1-\cos\theta)^2}\right]^3 \quad (4)$$

where ε is the surface porosity (varying from 0 and 1) and θ is the contact angle between the nucleus and the surface. θ is defined by the Young's equation:

$$\cos\theta = \frac{\gamma_{ls}-\gamma_{sn}}{\gamma_{\ln}} \quad (5)$$

with γ_{ln} the liquid−nucleus, γ_{ls} the liquid−surface, and γ_{sn} the surface −nucleus interfacial energies. As θ varies from 0° to 180°, the ratio $\Delta G^*_{HEN}/\Delta G^*_{HON}$ ranges between 0 and 1. Therefore, ΔG^*_{HEN} is always smaller than ΔG^*_{HON} which indicates that heterogeneous nucleation is always kinetically more favourable than homogeneous nucleation. Since accurate evaluation of θ is not trivial, we used the values of 139.5° and 136.4° measured for synthetic and real feed solutions, respectively, on hydrophobic polypropylene membrane of surface porosity 70%.

Although the calculated energy barrier for nucleation on the membrane is always lower than in the homogeneous case (Table 3), the values of ΔG^*_{HEN} are still several orders of magnitude higher than the thermal energy. This suggests that the formation of both *aragonite* and *halite* crystals recovered in the crystallization vessel is unlikely to be triggered by heterogeneous nucleation at the membrane surface[46], in agreement with recent studies that have shown that the nucleation mechanisms underlying bulk crystallization are distinct from nucleation within the solution/membrane boundary layer which could eventually lead to scaling[47].

Based on this assumption, we then calculated ΔG^*_{HEN} by considering heterogeneous nucleation on a solid and non-porous ($\varepsilon = 0$) surfaces which would be wetted ($\theta = 10°$) by the nascent nucleus. Table 3 contains such calculations where it is demonstrated that the nucleation energy barrier is typically comparable to or lower than the k_BT term, thus supporting the assumption that heterogeneous nucleation on exogenous solid surfaces is the main control of the nucleation step.

The data reported in Table 4 show that the waiting time estimated by turbidimetric monitoring, is between 35 and 96 min from the start of the

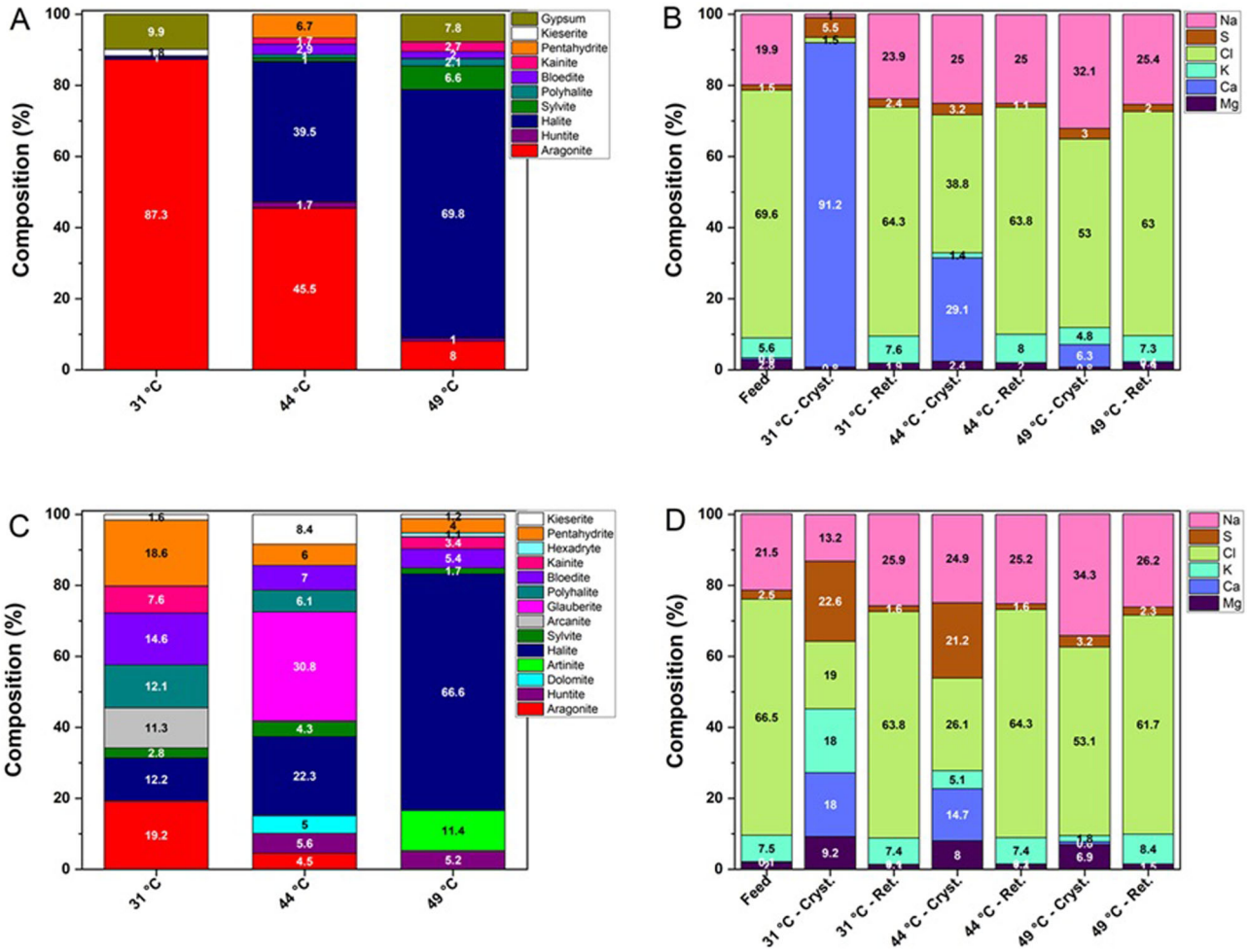

Fig. 6 | Quantitative composition of the solid precipitates for real solution. Composition obtained before (**A**, **B**) and after (**C**, **D**) basic treatment of real mine wastewater at different temperatures, in terms of crystalline phases detected by PXRD (**A**, **C**) and corresponding relative elemental composition (excluding C, O and H atoms) (**B**, **D**) in the starting solution (Feed), recovered crystals (Cryst.) and mother solution after removal of crystals by filtration (Ret.).

Table 3 | Free energy barrier of nucleation of *aragonite* and *halite* calculated for compositions of synthetic and real solutions at different crystallization temperatures, considering the homogeneous (HON) (Eq. 1) and heterogeneous (HEN) (Eq. 4) nucleation mechanism

		$\Delta G^*/k_BT$ (synt.)		$\Delta G^*/k_BT$ (real)		$\Delta G^*/k_BT$ (synt. BT)		$\Delta G^*/k_BT$ (real BT)	
	T (°C)	*Aragonite*	*Halite*	*Aragonite*	*Halite*	*Aragonite*	*Halite*	*Aragonite*	*Halite*
HON	31	5.55×10^4	1.22×10^4	8.44×10^4	N.D.	N.D.	3.69×10^3	2.20×10^4	N.D.
	44	4.69×10^4	2.03×10^4	6.90×10^4	N.D.	N.D.	4.50×10^3	1.77×10^4	N.D.
	49	4.77×10^4	1.84×10^3	6.75×10^4	4.97×10^4	N.D.	9.07×10^2	1.65×10^4	9.07×10^2
HEN ($\varepsilon = 0.7$)	31	5.15×10^4	1.13×10^4	7.58×10^4	N.D.	N.D.	3.41×10^3	1.97×10^4	N.D.
	44	4.33×10^4	1.88×10^4	6.20×10^4	N.D.	N.D.	4.16×10^3	1.59×10^4	N.D.
	49	4.40×10^4	1.70×10^3	6.06×10^4	4.46×10^4	N.D.	8.37×10^2	1.48×10^4	8.14×10^2
HEN ($\varepsilon = 0$; $\theta = 10°$)	31	9.55	2.10	14.5	N.D.	N.D.	0.64	3.78	N.D.
	44	8.08	3.50	11.9	N.D.	N.D.	0.78	3.05	N.D.
	49	8.21	0.32	11.6	8.55	N.D.	0.16	2.83	0.16

HEN was considered on porous ($\varepsilon = 0.7$) hydrophobic (θ: 139.5° with synthetic feed and 136.4° with real wastewater) membranes and on solid ($\varepsilon = 0$) hydrophilic (θ: assumed 10° with both synthetic and real solutions) surfaces (N.D. indicates that the solution is unsaturated with respect to that species).

experiments. Based on the measured transmembrane fluxes, this means that the solution concentration at which the first crystals were observed was 1–3% higher than at the initial feed. Since heterogeneous nucleation is generally initiated at low supersaturation[48], the experimental results support the possibility that heterogeneous mechanism was dominant in our MAC tests[49].

Figure 8 shows the composition of the crystalline precipitates with the saturation index of the corresponding species. It is notably that the species contained in larger quantities have *SI* values (calculated at the *CF* obtained at the end of the crystallization tests) around 0, while species with $SI \geq 1$ were rarely obtained. This is particularly evident for untreated and higher-

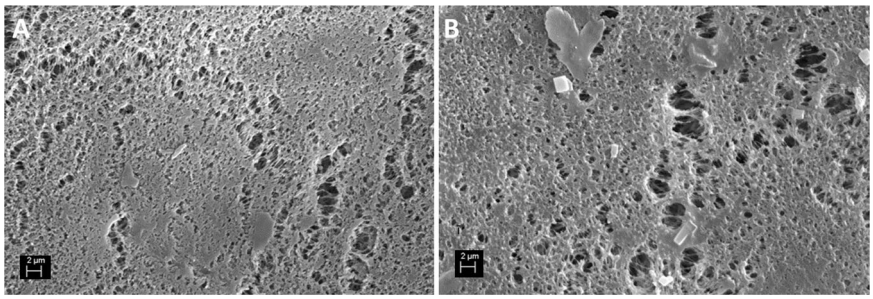

Fig. 7 | SEM micrographs of polypropylene membrane. Surface before MAC test (**A**) and after a crystallization test and rinsing with deionized water (**B**).

Table 4 | Average transmembrane flux (calculated from Eq. 7), waiting time detected by turbidimetric monitoring and solution concentration factor (*CF*) at the time of detection of the first nuclei, for different feed solutions and crystallization temperatures

Feed type	J_w (kg m^{-2} h^{-1})	Waiting time (min)	*CF* (@nucleation)
Synthetic 31–44 °C	1.92	96	1.03
Synthetic 49 °C	2.08	95	1.02
Synthetic BT 31–44 °C	2.08	60	1.03
Synthetic BT 49 °C	2.25	81	1.02
Real 31–44 °C	1.92	50	1.01
Real 49 °C	2.50	35	1.01
Real BT 31–44 °C	2.08	80	1.02
Real BT 49 °C	2.92	42	1.01

temperature solutions. Furthermore, solid phases characterized by a large negative *SI* (< -1) were accidentally observed only for pre-treated solutions and at the lowest temperature. Since *SI* values close to 0 are related to species of greater solubility (less stable), it is argued that the crystallization performed in our systems preferentially provides kinetic products in which metastable phases are the first to appear through a heterogeneous nucleation mechanism supported by exogenous solid surfaces dispersed in bulk solutions, while species with a strong thermodynamic tendency to precipitate are inhibited, due to solute depletion.

Furthermore, by comparing the crystallization results obtained under different conditions and theoretical predictions, it can be deduced that, while CNTs offer the starting point to describe the system studied, more sophisticated models are needed to define the complexity of the events related to nucleation in multi-ionic solutions such as hypersaline brines. The possibility that a system follows a specific path is difficult to predict with current knowledge, since the complex kinetics and numerous factors that govern the formation of metastable species driven by heterogeneous contributes pose a considerable difficulty in theoretical treatments.

In conclusion, this work demonstrated that within a relatively narrow range of operating temperatures, several crystalline salt minerals can be produced from real mine wastewater using MAC: at 31 °C, the solid product contained up to 87% by weight of $CaCO_3$ (and >91% in calcium) in the form of metastable polymorphic *aragonite*; with the operating temperature increased to 49 °C, the solid precipitate contained predominantly NaCl (~70%). Feed conditioning by basic pre-treatment was found to have a notable influence on the outcome of the crystallization process, being strongly dependent on the efficiency of Ca^{2+} ion removal. Experiments with synthetic brine have shown that quantitative removal of calcium allows the recovery of a precipitate containing 15% magnesium and 38% potassium.

Although our results are in accordance with recent studies demonstrating that the nucleation mechanisms underlying bulk crystallization in MAC are distinct from nucleation occurring in the boundary layer of the feed-membrane, heterogeneous nucleation effects mediated by dispersed impurity particles would affect the free energy barrier, thus allowing metastable or near-equilibrium species to precipitate soon after the solution begins to concentrate. These kinetic effects are believed to be at the origin of the inconsistencies between the theoretical prediction based on simulation work implemented on a purely thermodynamic ground and the observed composition of the solid products, calling for more sophisticated models to describe the complexity of the system.

Finally, based on the results of this work (process and conditions), we propose a new treatment scheme for the recovery of the valuable magnesium and potassium salts in a circular economy scenario, which can contribute to solving the problem of pollution resulting from mine tailing waste. The proposed approach represents an ecologically sustainable and technologically efficient process based on membrane-assisted crystallization, to be explored in the future on a larger scale to promote the green development of different industries.

Methods

Materials

Sodium chloride (NaCl, 27810.295, from VWR Chemicals), sodium hydrogen carbonate ($NaHCO_3$, 1.06329.1000, from Merck), sodium sulfate (Na_2SO_4, 13464, from Honeywell – Fluka), calcium chloride bihydrate ($CaCl_2{\cdot}2H_2O$, C/1500/53, from Fisher Scientific), magnesium chloride hexahydrate ($MgCl_2{\cdot}6H_2O$, 1.0583.1000, from Merck), potassium chloride (KCl, 26764.298, from VWR Chemicals) and magnesium sulfate heptahydrate ($MgSO_4{\cdot}7H_2O$, cod. 13142, from Honeywell—Fluka) were used as received to prepare synthetic hypersaline solutions of compositions reported in Table 5 (Synthetic). MilliQ water (0.05 µS/cm) was used to prepare artificial feed solutions and as condensing fluid on the distillate side in the MAC equipment. Commercial polypropylene (PP) membranes (Accurel PP 2E HF, nominal pore size 0.2 µm, overall porosity 70%) were purchased from Membrana GmbH (Wuppertal, Germany). The real mine tailing wastewater (Real) was collected from the brine collector in Castellgalí (Spain) and pre-filtered by PES membranes with nominal pore size of 0.45 µm prior to crystallization tests. Table 5 reports the ion concentration of both synthetic and real feed.

Simulations

Theoretical simulations were performed by PHREEQC (https://www.usgs.gov/software/phreeqc-version-3) software which generated the activity coefficient for high salinity solutions by implementing the Pitzer model[50]. The input parameters were the ion concentrations, temperature, density and pH of the feed solutions. The simulations provided saturation index (*SI*) curves as a function of solution concentration for the possible species that can form from the ionic combinations as the solvent is gradually removed from the initial solution.

The *SI* compares the ion activity product (*IAP*) with the solubility product (K_{sp}), based on the following relation:

$$SI = \log\left(\frac{IAP}{K_{sp}}\right) \quad (6)$$

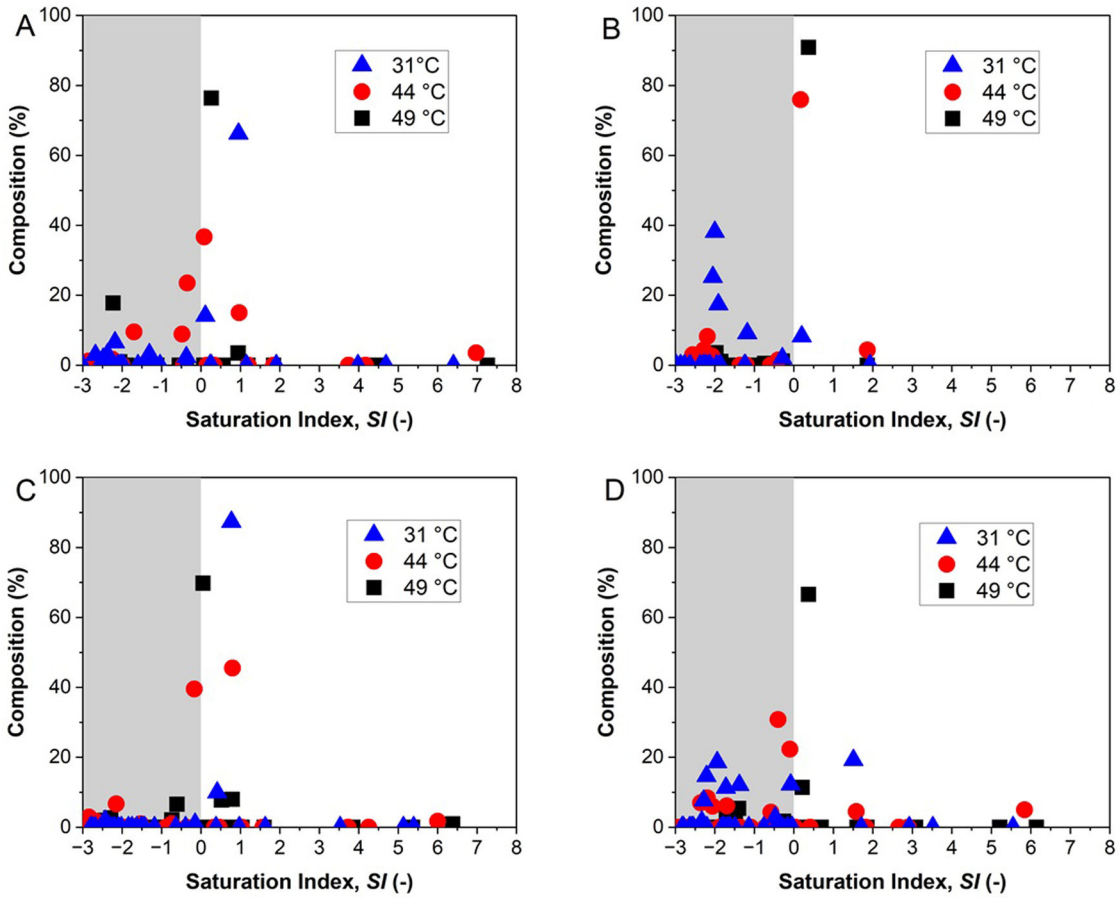

Fig. 8 | Saturation index for the main components of the solid precipitates. SI calculated at the effective concentration factors at the end of the crystallization tests for the component species and at the different temperatures, for hypersaline synthetic solution (**A**), synthetic solution after basic treatment (**B**), real wastewater from mines (**C**), real wastewater after basic treatment (**D**). The shaded areas highlight the negative SI region.

Table 5 | Composition for the feed solutions used in this work as measured by ion chromatography: synthetic hypersaline solution (Synthetic); synthetic solution after $CaCO_3$ precipitation by basic treatment (Synthetic BT); real mine tailing wastewater (Real); real mine tailing wastewater after basic treatment (Real BT)

Specie	Synthetic [mg/L]	Synthetic BT [mg/L]	Real [mg/L]	Real BT [mg/L]
Na^+	58,266	53,549	48,731	51,630
Mg^{2+}	7653	7570	6945	4930
Ca^{2+}	1281	<0.1	1405	271
K^+	18,999	16,863	13764	17,740
Cl^-	170,511	155,931	170,494	157,651
SO_4^{2-}	2499	1828	3709	5870
HCO_3^-	137	150	93	182
TDS	259,346	235,892	245,142	238,274
pH	7.4	7.7	7.5	7.8
density	1145	1163	1208	1202

SI values provide indications on the thermodynamic tendency of a certain specie to precipitate in the considered conditions: for $SI < 0$, Eq. 6 indicates that the solution is unsaturated with respect to that specie; for $SI > 0$, the solution is supersaturated and that specie is expected to crystallize. Therefore, *SI* values could help predict the solid phases emerging after crystallization as long as the solvent is removed across the membrane in the MAC process.

Membrane-assisted crystallization tests

The experimental lab-scale setup schematically illustrated in Fig. 9 consists of a nylon membrane module hosting a commercial hydrophobic flat sheet membranes with a total active area of 24 cm^2; a two-channel peristaltic pumps (Masterflex L/S digital drive, 7524-50, with easy-load pump heads, from Cole-Parmer, USA); two graduated cylinders for monitoring feed and distillate volume variations; three thermostatic baths (F32, Julabo, Germany) for the feed and distillate side; a technical balance to measure the increase in distillate weight due to water recovery from the feed; on-line conductivity sensors (CONDS-N-025, PendoTECH, USA) placed at the outlet of the membrane module and connected to a datalogger (CMONT, PendoTECH, USA); K-type thermocouples connected, to a multi-channel thermometer (SPER Scientific, 800024), to read temperature at the inlet and the outlet of the membrane module and within the distillate and feed solutions vessels; pressure sensors (PREPS-N-025, from PendoTECH, USA) connected to a monitor (PMAT2A, from PendoTECH, USA), to measure pressure at the inlet of the feed and distillate of the membrane module; a turbidity measurement system consisting of a compact on-line UV-VIS-NIR 280–880 nm dual-wavelength photometer (SPEC-L-2-280-880-PHOTO, from PendoTECH, USA) with a flow cell having 1 cm path length (SPECPS-N-025, from PendoTECH, USA) integrated into the feed line and directly connected to the photometer by fiber optics and a monitor (PMAT2A). Turbidity monitoring allows to detect the waiting time for crystallization, indicating the elapsed time between the creation of the supersaturation and the appearance of the first detectable nuclei. The flow

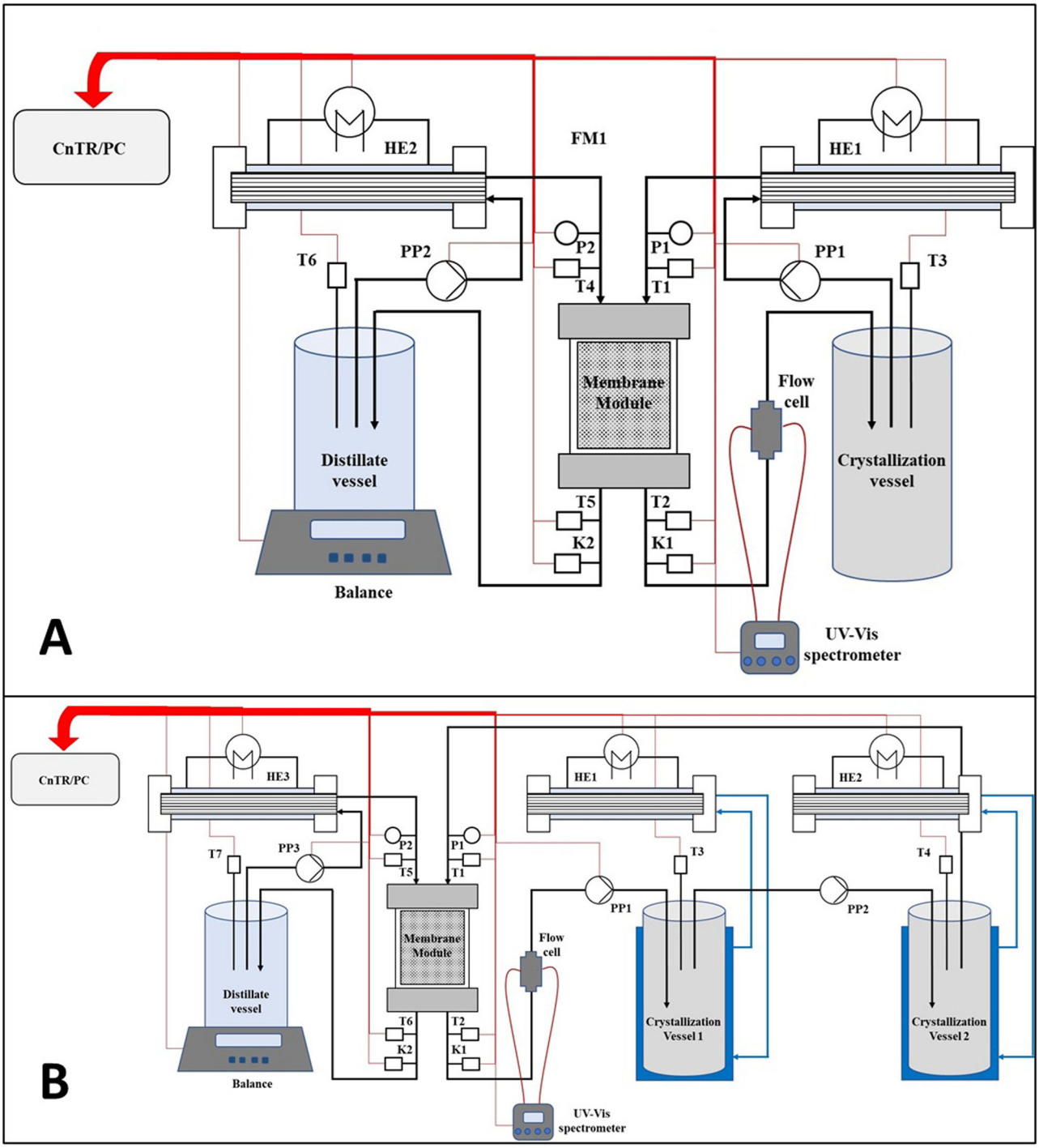

Fig. 9 | Schematic representation of the MAC equipment. Experiments performed with two different configurations: feed solution is circulated at constant temperature of 49 °C (**A**); the feed solution line is broken down in two crystallization stages working at the same concentration factor but different temperature: 31 °C and 44 °C (Tx: temperature probes; Kx: conductivity probes; Px: pressure sensors; PPx: peristaltic pumps; HEx: heat exchangers; CnTR/PC: programmable logic controller connected to a PC) (**B**).

rate was set at 60 mL/min ($v = 4.8\times10^{-3}$ m s^{-1}) for both feed and distillate solutions to allow working in laminar regime (*Re* around to 30). Based on preliminary experiments, this fluid dynamic condition represents a compromise that allows a moderate transmembrane flux associated with a supersaturation generation rate that avoids excessive nucleation and a retention time that allows crystallization in a time interval of 24–28 h.

Experiments were performed by using the two MAC equipment configurations showed in Fig. 9; in Fig. 9A, the feed and the distillate solutions, with a starting volume of 0.25 L each, were circulated at a nominal temperature of 49 °C and 10 °C, respectively (further details can be found elsewere[51]). In Fig. 9B, the feed line was broken down into two crystallization chambers working at different temperature: 31 °C and 44 °C. This approach allowed to differentiate the crystallization at the two temperatures while keeping the same concentration factor in both vessels.

MAC tests were performed with hypersaline artificial or real mine tailing wastewater before and after basic treatment (BT), having the ion compositions reported in Table 5.

The pH and conductivity of the feed and distillate prior the tests and at the end of the MAC experiments were measured by a pH/conductivity meter (Orion Star A215, from Thermo Scientific). The water transmembrane flux J_w [kg m^{-2} h^{-1}] was evaluated by monitoring the increase in the distillate weight every 30 min and taken as the average value under steady conditions (normally after the first hour of operation), calculated as:

$$J_w = \frac{\Delta M_d}{\Delta t \cdot A_m} \quad (7)$$

where ΔM_d [kg] is the increment in mass of distillate, Δt [h] is the distillation time and A_m [m^2] is the active membrane area. The solute rejection R [%] was determined as:

$$R = \left(1 - \frac{C_d}{C_f}\right) \cdot 100 \quad (8)$$

where C_d and C_f [g L^{-1}] are the distillate and the feed salt concentrations, respectively, that were estimated after mass balance by measuring the electrical conductivity of the solutions. Each MAC test lasted 28 h.

Optical microscopy

At time intervals of 6, 24 and 28 h, a sample (0.5 mL) of the feed was withdrawn from the crystallization vessel(s) and visually examined by optical microscope (Eclipse LV100ND, from Nikon) to determine the crystal size distribution (*CSD*). At the end of the tests, crystals were recovered by vacuum filtration using a polyethersulfone (PES) membrane (Durapes, nominal pore size 0.2 µm, from Membrana GmbH, Wuppertal, Germany), washed with ethanol, dried in a thermobalance to estimate the amount of crystal recovered per unit volume of mother liqueur (magma density), and then stored in a desiccator before powder X-ray diffraction (PXRD) analyses. The crystal size distribution was calculated by processing the pictures by using the ImageJ software. The coefficient of variation (*CV*), representing the dispersion of the size distribution curve around the mean size, was calculated by the following relation:

$$CV = \frac{L_{84\%} - L_{16\%}}{2 \cdot L_{50\%}} \quad (9)$$

where L is the crystal size as in the F(L) curve at the specified percentage[52].

Scanning electron microscopy (SEM)

A qualitative characterization of crystals was carried out by scanning electron microscopy (SEM) (Pro X desktop SEM from Phenom) equipped with a backscattering detector (BSD-Phenom-World B.V., Eindhoven, the Netherlands). Prior of SEM analyses, all samples were sputter-coated (1 min cycle) with a thin layer of gold using a Quorum Q150 RS sputter machine (Quorum Technologies Ltd, Ashford, Kent, England) to minimize the charge and improve the image quality. Elemental analyses were performed with an energy dispersive X-ray spectroscopy detector (EDX) and the Phenom Elemental Mapping Software.

Ion chromatography (IC)

To quantify ion composition, the starting feed solutions and dissolved solid precipitates obtained from experiments were analyzed by ionic chromatography (Dionex Integrion HPIC from Thermo Fisher Scientific, USA) equipped with a conductimetric detector. Anion's concentration was determined using a Dionex IonPac™ AS22-Fast-4 µm 2x150 mm analytical column with suppressor (Dionex AERS 500 carbonate 2 mm) and sodium carbonate/sodium bicarbonate solution as eluent. Cation analysis were performed by a Dionex IonPac™ CS16-Fast 4 µm analytical column with suppressor (Dionex CERS 500, 2 mm) and methanesulfonic acid as eluent. Before analysis, samples were filtered with 0.45 µm pore size PES membrane and subsequently diluted to the desired concentration range with MilliQ water.

Qualitative and quantitative powder X-ray diffraction analysis

Powder X-ray diffraction (PXRD) profiles were collected by using a Rigaku Rint2500 laboratory diffractometer with a rotating Cu anode. The instrument operated at 50 kV and 200 mA in Debye-Scherrer geometry. The diffractometer is equipped with an asymmetric Johansson Ge (111) crystal to select the monochromatic Cu$K_{\alpha 1}$ radiation (λ = 1.54056 Å) along with the silicon strip Rigaku D/teX Ultra detector. The data were collected in the range of 5 to 100° (2ϑ) with a step size of 0.02° (2ϑ) and a counting time of 6 s/step. To perform the measurements, each powder sample was introduced in a glass capillary with a diameter of 0.5 mm and mounted on the goniometer's axis. The capillary was rotated during the measurement to enhance the randomization of the individual crystallites' orientations and minimize the potential impact of preferred orientation.

As a first step, collected PXRD profiles were processed with the computer program QualX2.0[53] to perform crystal phase(s) identification. The software can query the commercial PDF-2 database[54] and the freely available POW_COD database. QualX2.0 searches for the phase(s) belonging to the database best matching the experimental pattern, *via* a search/match approach using the list of experimental values of interplanar *d*-spacings (derived from the diffraction angle) and peak intensities.

As a second step, the crystal phases identified by qualitative analysis were used to perform quantitative analysis. Given the number of crystal phases present for each brine mixture, this was performed by using two different approaches: the Rietveld refinement process using the EXPO software[55], which was used to validate the crystal phase composition and to perform a graphic inspection of the differences between measured and calculated profiles, and the computer program QUANTO[56], which was used for robust weight fraction assessment on selected crystal phases.

The main difficulties encountered were the complexity of crystal phase composition of the brine mixtures and the prevalence of the NaCl phase in most of them, which hides the signal coming from the minority phases in the diffraction profile.

Data availability

The data supporting the key findings of this study are available within the article and by the repository ZENODO.

Received: 4 August 2024; Accepted: 11 October 2024;
Published online: 09 November 2024

References

1. Dong, L. et al. Some developments and new insights of environmental problems and deep mining strategy for cleaner production in mines. *J. Clean. Prod.* **210**, 1562–1578 (2019).
2. Martins, F. F. & Castro, H. Raw material depletion and scenario assessment in European Union – a circular economy approach. *Energy Rep.* **6**, 417–422 (2020).
3. Dolgin, E. Water and Warfare: The Battle to Control a Precious Resource. *Nature* (2023), https://doi.org/10.1038/d41586-023-03883-w.
4. Angelakis, A. N., Tzanakakis, V. A., Capodaglio, A. G. & Dercas, N. A Critical Review of Water Reuse: Lessons from Prehistoric Greece for Present and Future Challenges. *Water* **15**, 2385 (2023).
5. Upadhyay, A., Laing, T., Kumar, V. & Dora, M. Exploring barriers and drivers to the implementation of circular economy practices in the mining industry. *Resour. Policy* **72**, 102037 (2021).
6. The Role of Critical Minerals in Clean Energy Transitions, IEA, Paris (2021) https://www.iea.org/reports/the-role-of-critical-minerals-in-clean-energy-transitions
7. Global Tailings Review. Towards Zero Harm: A Compendium of Papers. Chapter II Mine Tailings Facilities: Overview and Industry Trends (2022) https://globaltailingsreview.org/compendium

8. Hatje, V. et al. The environmental impacts of one of the largest tailing dam failures worldwide. *Sci. Rep.* **7**, 10706 (2017).
9. Smith, V. H., Tilman, G. D. & Nekola, J. C. Eutrophication: impacts of excess nutrient inputs on freshwater, marine, and terrestrial ecosystems. *Envir. Poll.* **100**, 179–196 (1999).
10. Shrivastava, P. & Kumar, R. Soil salinity: A serious environmental issue and plant growth promoting bacteria as one of the tools for its alleviation. *Saudi J. Biol. Sci.* **22**, 123–131 (2015).
11. Fontananova, E., Grosso, V., Pantuso, E., Donato, L. & Di Profio, G. Energy duty in direct contact membrane distillation of hypersaline brines operating at the water-energy nexus. *J. Memb. Sci.* **676**, 121585 (2023).
12. Belhout, D., Tigrine, Z., Mosnegutu, E. F. & Benabdelaziz, F. K. Management of reverse osmosis concentrate by solar distillation. *Water Supply* **22**, 6490–6503 (2022).
13. Morgante, C. et al. Influence of Operational Strategies for the Recovery of Magnesium Hydroxide from Brines at a Pilot Scale. *Ind. Eng. Chem. Res.* **61**, 15355–15368 (2022).
14. Avci, A. H. et al. Energy Harvesting from Brines by Reverse Electrodialysis Using Nafion Membranes. *Membranes* **10**, 168 (2020).
15. Tufa, A. R. et al. Integrated membrane distillation-reverse electrodialysis system for energy-efficient seawater desalination. *Appl. Energy* **253**, 113551 (2019).
16. Ji, X. et al. Membrane distillation-crystallization of seawater reverse osmosis brines. *Sep. Purif. Tech.* **71**, 76–82 (2010).
17. Loganathan, P., Naidu, G. & Vigneswaran, S. Mining valuable minerals from seawater: a critical review. *Environ. Sci. Water Res. Technol.* **3**, 37–53 (2017).
18. Chen, G., Lu, Y., Krantz, W. B., Wang, R. & Fane, A. G. Optimization of operating conditions for a continuous membrane distillation crystallization process with zero salty water discharge. *J. Memb. Sci.* **450**, 1–11 (2014).
19. Mohammad, A. F., El-Naas, M. H., Al-Marzouqi, A. H., Suleiman, M. I. & Al Musharfy, M. Optimization of Magnesium Recovery from Reject Brine for Reuse in Desalination Post-Treatment. *J. Water Proc. Eng.* **31**, 100810 (2019).
20. Casas, S. et al. Valorisation of Ca and Mg By-Products from Mining and Seawater Desalination Brines for Water Treatment Applications. *J. Chem. Technol. Biotechnol.* **89**, 872–883 (2014).
21. Cipollina, A. et al. Reactive crystallisation process for magnesium recovery from concentrated brines. *Des. Water Treat.* **55**, 2377–2388 (2015).
22. Drioli, E., Di Profio, G. & Curcio, E. Membrane-Assisted Crystallization Technology, Advances in Chemical and Process Engineering: Volume 2 (2015), World Scientific. ISBN: 978-1-78326-331-8, https://doi.org/10.1142/p912.
23. Deshmukh, A. et al. Membrane distillation at the water-energy nexus: limits, opportunities, and challenges. *Energy Environ. Sci.* **11**, 1177–1196 (2018).
24. Ruiz Salmón, I. & Luis, P. Membrane crystallization via membrane distillation. *Chem. Eng. Process. Proc. Inten.* **123**, 258–271 (2018).
25. Kim, J., Park, K., Yang, D. R. & Hong, S. A comprehensive review of energy consumption of seawater reverse osmosis desalination plants. *Appl. Energy* **254**, 113652 (2019).
26. Drioli, E., Di Profio, G. & Curcio, E. Progress in membrane crystallization. *Curr. Opin. Chem. Eng.* **1**, 178–182 (2012).
27. Di Profio, G., Curcio, E. & Drioli, E. Membrane Crystallization Technology in Comprehensive Membrane Science and Engineering. Eds. Drioli, E. Giorno, L. 2010, 21-46 Elsevier https://doi.org/10.1016/B978-0-08-093250-7.00018-9.
28. Ruiz Salmón, I., Simon, K., Clèrin, C. & Luis, P. Salt recovery from wastewater using membrane Distillation-Crystallization. *Cryst. Growth Des.* **18**, 7275–7285 (2018).
29. Bouchrit, R. et al. Membrane crystallization for mineral recovery from saline solution: Study case Na_2SO_4 crystals. *Desalination* **412**, 1–12 (2017).
30. Gómez, J. et al. Recovery of copper sulfate from acidic mine waters by membrane crystallization. *J. Memb. Sci.* **700**, 12270 (2024).
31. Alessandro, F., Macedonio, F., Frappa, M. & Drioli, E. Freshwater and minerals recovery from synthetic produced water by membrane distillation/membrane crystallization processes. *Appl. Water Sci.* **14**, 104 (2024).
32. Pokrovsky, O. S. & Schott, J. Experimental study of brucite dissolution and precipitation in aqueous solutions: surface speciation and chemical affinity control. *Geochim. Cosmoch. Acta* **68**, 31–45 (2004).
33. Politi, Y. et al. Sea Urchin Spine Calcite Forms via a Transient Amorphous Calcium Carbonate Phase. *Science* **306**, 1161 (2004).
34. De Choudens-Sánchez, V. & González, L. A. Calcite and aragonite precipitation under controlled instantaneous supersaturation: Elucidating the role of $CaCO_3$ saturation state and Mg/Ca ratio on calcium carbonate polymorphism. *J. Sediment. Res.* **79**, 363–376 (2009).
35. Morse, J. W., Wang, Q. & Tsio, M. Y. Influences of temperature and Mg:Ca ratio on $CaCO_3$ precipitates from seawater. *Geology* **25**, 85–87 (1997).
36. Morse, J. W., Arvidson, R. S. & Lüttge, A. Calcium carbonate formation and dissolution. *Chem. Rev.* **107**, 342–381 (2007).
37. Navrotsky, A. Energetic clues to pathways to biomineralization: Precursors, clusters, and nanoparticles. *Proc. Natl Acad. Sci. USA* **101**, 12096–12101 (2004).
38. Sun, W., Jayaraman, S., Chen, W., Persson, K. A. & Ceder, G. Nucleation of metastable aragonite $CaCO_3$ in seawater. *Proc. Natl Acad. Sci. USA* **112**, 3199–3204 (2015).
39. Gibbs, J. W. On the equilibrium of heterogeneous substances. *Trans. Connect. Acad. Arts Sci.* **3**, 108–248 (1879). and 343–524.
40. Karthika, S., Radhakrishnan, T. & Kalaichelvi, P. A review of classical and nonclassical nucleation theories. *Cryst. Growth Des.* **16**, 6663–6681 (2016).
41. De Yoreo, J. J. et al. Crystallization by particle attachment in synthetic, biogenic, and geologic environments. *Science* **349**, 6760v (2015).
42. Cedeno, R. et al. CNT effective interfacial energy and pre-exponential kinetic factor from measured NaCl crystal nucleation time distributions in contracting microdroplets. *J. Chem. Phys.* **158**, 194705 (2023).
43. Kashchiev, D. Thermodynamically consistent description of the work to form a nucleus of any size. *J. Chem. Phys.* **118**, 1837–1851 (2003).
44. Liu, X. Y. Heterogeneous nucleation or homogeneous nucleation? *J. Chem. Phys.* **112**, 9949–9955 (2000).
45. Curcio, E., Fontananova, E., Di Profio, G. & Drioli, E. Influence of the structural properties of poly (vinylidene fluoride) membranes on the heterogeneous nucleation rate of protein crystals. *J. Phys. Chem. B* **110**, 12438–12445 (2006).
46. Christie, K. S. S. et al. Gypsum scaling in membrane distillation: Impacts of temperature and vapor flux. *Desalination* **525**, 115499 (2022).
47. Jikazana, A., Campo, P. & McAdam, E. J. Hydrodynamics (Reynolds number) determine scaling, nucleation and crystal growth kinetics in membrane distillation crystallisation. *J. Memb. Sci.* **685**, 121909 (2023).
48. Söhnel, O. & Mullin, J. W. A method for the determination of precipitation induction periods. *J. Cryst. Growth* **44**, 377–382 (1978).
49. Jikazana, A. et al. The role of mixing on the kinetics of nucleation and crystal growth in membrane distillation crystallisation. *Sep. Purif. Techn.* **353**, 128533 (2025).
50. Pitzer, K. S. Thermodynamics of electrolytes. I. Theoretical basis and general equations. *J. Phys. Chem.* **77**, 268–277 (1973).
51. Di Profio, G., Tucci, S., Curcio, E. & Drioli, E. Controlling Polymorphism with Membrane-Based Crystallizers: Application to Form I and II of Paracetamol. *Chem. Mater.* **19**, 2386–2388 (2007).
52. Garside, J., Mersmann, A. & Nyvlt, J. Measurement of Crystal Growth and Nucleation Rates, 2nd Ed., IChemE, Rudby, 2002, ISBN: 0852954492, 9780852954492.
53. Altomare, A. et al. QUALX2.0: a qualitative phase analysis software using the freely available database POW_COD. *J. Appl. Crystallogr.* **48**, 598–603 (2015).

54. ICDD. The Powder Diffraction File. International Center for Diffraction Data, 12 Campus Boulevard, Newton Square, Pennsylvania 19073-3273, USA, 2003.
55. Altomare, A. et al. The Rietveld refinement in the EXPO software: a powerful tool at the end of the elaborate crystal structure solution pathway. *Crystals* **8**, 203 (2018).
56. Altomare, A. et al. Quanto: a Rietveld program for quantitative phase analysis of polycrystalline mixtures. *J. Appl. Crystallog.* **34**, 392–39 (2001).

Acknowledgements

Authors would like to thank Soriguè-Acsa company (Spain) for providing mine-tailing wastewater samples from the Castellgalì site. This work has received funding from the European Union's Horizon 2020 research and innovation programme within the IntelWATT project, under grant agreement n. 958454 (http://www.intelwatt.eu/).

Author contributions

Conceptualization: G.D.P. and E.F.; funding acquisition: E.F.; data curation: E.P., L.D., R.R., R.C.; investigation: E.P, L.D., R.R.; methodology: G.D.P.; supervision: G.D.P. and R.C.; validation: L.D., E.E., R.R.; visualization: G.D.P., R.C.; writing – original draft: G.D.P., E.P.; writing - review & editing: G.D.P., E.F., R.C, R.R.

Competing interests

The authors declare no competing interests.

Additional information

Correspondence and requests for materials should be addressed to Enrica Fontananova or Gianluca Di Profio.